PCCP

# First-Principles Prediction of Electronic Structure and Optoelectronic Properties of Degenerate p-Type Alloyed $CsPb_{1-x}Cu_xBr_3$ Perovskite System

SCHOLARONE™
Manuscripts

## Guidelines for Reviewers

Thank you very much for agreeing to review this manuscript for _Journal of Materials Chemistry C_.

_Journal of Materials Chemistry C_ is a weekly journal in the materials field. The journal is interdisciplinary, publishing work of international significance on all aspects of materials chemistry related to applications in optical, magnetic and electronic devices. Articles cover the fabrication, properties and applications of materials.

_Journal of Materials Chemistry C_'s Impact Factor is **6.4** (2022 Journal Citation Reports®)

---

_The following manuscript has been submitted for consideration as a_

## FULL PAPER

---

For acceptance, a Full paper must report primary research that demonstrates significant **novelty and advance**, either in the chemistry used to produce materials or in the properties/ applications of the materials produced. Work submitted that is outside of these criteria will not usually be considered for publication. The materials should also be related to the theme of optical, magnetic and electronic devices.

When preparing your report, please:
- Focus on the **originality**, **importance**, **impact** and **reproducibility** of the science.
- Refer to the **journal scope and expectations**.
- **State clearly** whether you think the article should be accepted or rejected and give detailed comments (with references) both to help the Editor to make a decision on the paper and the authors to improve it.
- **Inform the Editor** if there is a conflict of interest, a significant part of the work you cannot review with confidence or if parts of the work have previously been published.
- **Provide your report rapidly** or inform the Editor if you are unable to do so.

**PLEASE NOTE:** _Journal of Materials Chemistry C_ offers authors the option of transparent peer review (TPR). If authors choose TPR, the reviewers' comments, authors' response and editor's decision letter for all stages of review are also published if the article is accepted. Reviewers will remain anonymous unless they choose to sign their report and only comments to the authors will be published – confidential comments to the editor will not be published.

Please note by peer reviewing you give consent to your anonymised report being published if authors have selected TPR.

Best regards,

**Professor Natalie Stingelin**
Editor-in-Chief
Georgia Institute of Technology, USA

**Dr Michaela Mühlberg**
Executive Editor
Royal Society of Chemistry

Contact us

Please visit our reviewer hub for further details of our processes, policies and reviewer responsibilities as well as guidance on how to review, or click the links below.

What to do when you review

Reviewer responsibilities

Process & policies

Dear editors and referees,

We would like to submit our paper entitled "**First-Principles Prediction of Electronic Structure and Optoelectronic Properties of Degenerate p-Type Alloyed CsPb$_{1-x}$Cu$_x$Br$_3$ Perovskite System**" for consideration for publication in *Physical Chemistry Chemical Physics*.

The application of non-toxic and lead-free metal halide perovskites in photovoltaic and optoelectronic devices has sparked widespread interest. Among various candidates, copper-based halide perovskite materials, characterized by their low cost, stability and eco-friendliness, have drawn considerable attention. In this study we will analyze the optoelectronic and carrier transport properties of the lead-copper alloying system CsPb$_{1-x}$Cu$_x$Br$_3$(x = 0, 0.125, 0.25, 0.5, 0.75, 1). The goal is to *predict a low-toxicity, low-cost copper-based 3D perovskite with controlled doping and tunable energy band for efficient and reliable hole transport and light absorption materials of perovskite solar cells*, by utilizing first-principles calculations based on density functional theory (DFT). Our research results also provide a theoretical foundation for the design of new functional perovskite materials with unique optoelectronic characteristics.

I would like to declare on behalf of my co-authors that the work described was original research that has not been published previously, and is not under consideration for publication elsewhere, in whole or in part. All the authors listed have approved the manuscript that is enclosed.

Thanks a lot for your time. We are looking forward to hearing from you.

Kind regards,

Professor Dr. Yu Qiu

*Key Laboratory of Green Perovskites Application of Fujian Province Universities*
*Fujian Jiangxia University*
*Fuzhou 350108, China*
*Tel: +86-591-23531356, Fax: +86-591-23531375*
*E-mail: yuqiu@fjjxu.edu.cn*

# First-Principles Prediction of Electronic Structure and Optoelectronic Properties of Degenerate p-Type Alloyed CsPb$_{1-x}$Cu$_x$Br$_3$ Perovskite System

Jiaming Huang, Linqin Jiang[*], Jiansen Wen, Baisheng Sa, Bo Wu[*], Jiansheng Li, Ping Li, Hao Xiong, Yu Qiu[*]
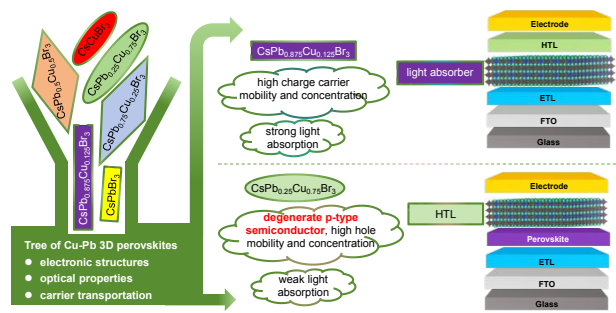


- First-principles calculations of structure-properties relationship reveal degenerate p-type semiconducting nature of alloyed CsPb$_{1-x}$Cu$_x$Br$_3$ for PSCs' absorber and transport layer.

# First-Principles Prediction of Electronic Structure and Optoelectronic Properties of Degenerate p-Type Alloyed CsPb$_{1-x}$Cu$_x$Br$_3$ Perovskite System

Jiaming Huang[1], Linqin Jiang[2*], Jiansen Wen[1], Bo Wu[1*], Baisheng Sa[1], Jiansheng Li[3], Ping Li[2], Hao Xiong[2], Yu Qiu[2*]

[1] *School of Materials Science and Engineering & School of Advanced Manufacturing, Fuzhou University, Fuzhou 350108, China*

[2] *Key Laboratory of Green Perovskites Application of Fujian Province Universities, Fujian Jiangxia University, Fuzhou 350100, China*

[3] *National PV Industry Measurement and Testing Center, Fujian Metrology Institute, Fuzhou 350003, China*

\* Corresponding Authors. *E-mail addresses: linqinjiang@fjjxu.edu.cn (L. Jiang), wubo@fzu.edu.cn (W. Bo), yuqiu@fjjxu.edu.cn (Y. Qiu).*

## ABSTRACT

The application of non-toxic and lead-free metal halide perovskites in photovoltaic and optoelectronic devices has sparked widespread interest. Among various candidates, copper-based halide perovskite materials, characterized by their low cost, stability and eco-friendliness, have drawn considerable attention. In this study, starting from the cubic structure of CsPbBr$_3$, the structural, electronic, optical, and charge carrier transport properties of the lead-copper alloying CsPb$_{1-x}$Cu$_x$Br$_3$ system were analyzed using density functional theory (DFT) based on first-principles calculations. Electronic structure calculations indicate that as-designed new 3D Cu-alloyed perovskite system exhibit characteristics of p-type degenerate semiconductors. We further comprehensively analyzes optoelectronic performance and charge carrier transport properties of Cu-alloyed samples. The results suggest that CsPb$_{0.875}$Cu$_{0.125}$Br$_3$ is a promising candidate for the absorber layer in perovskite solar cells (PSCs) due to its high charge carrier mobility and strong light absorption as a direct bandgap semiconductor. On the other hand, CsPb$_{0.25}$Cu$_{0.75}$Br$_3$, characterized as a p-type indirect bandgap semiconductor with a significantly higher hole mobility than electron mobility, along with weak sunlight absorption, is suitable for hole transport layer fabrication in PSCs.

# 1.Introduction

Metal halide perovskites, as members of the semiconductor family, have garnered widespread attention among researchers. The chemical formula for metal halide cubic perovskites is typically represented as $ABX_3$, where A is a cation, B is a divalent metal cation, and X is a halide anion. Metal halide perovskites exhibit numerous outstanding optoelectronic properties, including high optical absorption, extended charge diffusion length, excellent charge carrier mobility, and low excitation formation enthalpy[1-5]. Due to these unique properties, it has found widespread applications in the field of optoelectronics, such as light-emitting diodes and solar cells[6]. As of now, the power conversion efficiency (PCE) of single-junction perovskite solar cells (PSCs) has reached 26.1%[10]. However, achieving high PCE relies on the synergy between various functional layers of PSC. P-type semiconductors, commonly employed as hole transport materials (HTMs), play a crucial role as one of these functional layers. They extract and transport holes from the perovskite layer to the respective electrodes, facilitating the separation of electron-hole pairs and suppressing their recombination. The concentration and mobility of hole carriers directly influence the key optoelectronic properties of p-type semiconductors. Currently, organic materials are widely used as HTMs and have achieved considerable efficiency[11]. However, their complex synthesis and purification processes, along with poor thermal and chemical stability, result in high production costs and short device lifetime, significantly hindering the large-scale commercialization of perovskite solar cells. Alternative inorganic HTMs have made significant strides in addressing the stability and cost challenges of organic materials, but their properties remains limited. Therefore, the development of a new generation of inorganic p-type semiconductors with high hole mobility and stability is of great significance and urgency for future mass production of PSCs.

$CsPbBr_3$ is a prevalent all-inorganic metal halide perovskite, characterized by a direct bandgap structure, high absorption coefficient, small hole and electron effective masses, as well as high stability[12]. Furthermore, $CsPbBr_3$ is a weakly p-type material, but its carrier concentration is low due to the Fermi level remaining several hundred meV above the valence band maximum (VBM)[15-16]. To work as a high performance HTM, the essential need is to find more effective and reliable dopants[17]. Researchers

2

have found that substituting metal elements for lead can achieve acceptor doping. Transition metals like Fe, Cu, and Zn may be an excellent option to replace toxic Pb in perovskite structures due to their cost-effectiveness, environmentally benign and less toxic nature[19]. Especially, copper is considered one of the promising candidates for forming p-type doping materials as a substitute for lead[20].

Recently, copper halide perovskites (CHPs) have emerged as promising alternatives to lead halide perovskites, experiencing vibrant development. This is attributed to their intrinsic characteristics, including low production costs, high environmental stability, diverse crystal structures, and excellent optoelectronic properties[25]. Depending on the oxidation state of the Cu element, the structure of CHPs can be roughly divided into two categories[30]. Cu(I)-based CHP materials typically exhibit low-dimensional structures, such as $Cs_3Cu_2X_5$ (0D), $CsCu_2X_3$ (1D), and $(CH_3NH_3)_2CuX_4$ (2D), where X represents Cl, Br, or I elements. Due to the structural differences between these low-dimensional copper-based halides and traditional perovskites, some scholars consider them derivatives of perovskites, also known as ternary copper halides (TCHs)[31]. Cu(II)-based CHPs typically exhibit three-dimensional structures, such as $CsCuBr_3$[32]. Except for this one, there are almost no other reports on 3D-structured CHPs. With intensive research activity, the luminescence efficiency of low-dimensional TCHs can rival that of most lead halide perovskites, achieving significant breakthroughs in optoelectronic device manufacturing[33]. However, compared to 3D CHPs, low-dimensional TCHs typically suffer from defects such as larger electron/hole effective masses and lower charge carrier mobilities[36], which are unfavorable for charge transport. Drawing from the mature experience of lead halide perovskites, doping or alloying may be a promising approach to modulating the electronic dimensions of 3D CHPs[38].

Herein, we start from the 3D cubic structure of $CsPbBr_3$ in order to design alloyed CHPs for efficient light absorption and hole transportation in perovskite solar cells. By utilizing first-principles calculations based on density functional theory (DFT), we will analyze the optoelectronic and carrier transport properties of the lead-copper alloying system $CsPb_{1-x}Cu_xBr_3$. The goal is to predict a low-toxicity, low-cost copper-based 3D perovskite with controlled doping and tunable energy band for efficient and reliable HTLs in optoelectronic devices. Our research results will also provide a theoretical foundation for the design of CHP devices and the enhancement of their photovoltaic performance.

## 2. Computational methods

In this paper, the Vienna Ab initio Simulation Package (VASP) under the framework of density functional theory was employed for theoretical calculation and analysis. We use the generalized gradient approximation (GGA) within the Perdew-Burke-Ernzerhof (PBE) functional for exchange-correlation interactions. As is well known, the GGA-PBE method lacks sufficient accuracy when calculating strongly correlated electronic systems with d or f orbitals, often resulting in underestimated band gaps. More advanced methods, such as the many-body perturbation theory based on the Green's function and screened Coulomb interaction (GW method) and Heyd-Scuseria-Ernzerhof (HSE) hybrid density functional, offer higher precision. However, the computational cost of these methods is prohibitively high and is limited to systems with few atoms[39]. Additionally, when describing electronic orbitals containing heavy metal ions (such as Pb), spin-orbit coupling (SOC) effects are typically considered[42]. This effect alters the electronic band structure and occupancy states, influencing the variation of the band gap. Other studies have also shown that the SOC effect has a significant impact on the band dispersion and transport properties[44].

To simultaneously balance computational resources and accuracy, this study employed both the GGA-PBE and GGA-PBE+SOC methods to describe the electronic structure of $CsPb_{1-x}Cu_xBr_3$ (x = 0, 0.125, 0.25, 0.5, 0.75, 1) and conducted a comparative analysis. Considering the focus of this paper on the trend of the bandgap in Cu-alloying systems, the HSE method was not used for precise bandgap calculations. The atomic pseudopotential was described by the projector augmented wave method (PAW). In order to better describe the $CsPb_{1-x}Cu_xBr_3$ system, we constructed a $2 \times 2 \times 2$ supercell containing 40 atoms, as shown in Fig. 1. Electronic orbitals have been set as Cs $5s^25p^66s^1$, Pb $6s^26p^2$, Cu $3d^{10}4s^1$, and Br $4s^24p^5$. In this theoretical approach, the cutoff energy, the convergence accuracy, and the residual force are set to 400 eV, $1 \times 10^{-6}$ eV per atom and 0.02 eV, respectively[44]. Brillouin zone integration is performed with $5 \times 5 \times 5$ k-points and $11 \times 11 \times 11$ k-points employing the Monkhors-Pack technique for the Pb-Cu alloyed $CsPb_{1-x}Cu_xBr_3$ and pure $CsPbBr_3$ samples, respectively.

4

# 3. Results and discussion

## 3.1. Structural properties and phase stability

The $CsPbBr_3$ crystal exhibits various space groups, including Pnma, Amm2, pm-3m, etc. The focus of this study is on the cubic structure of the $CsPbBr_3$ crystal belonging to the pm-3m (No. 221) space group. The primitive cell is depicted in Fig. 1(a), comprising 1 Cs, 1 Pb, and 3 I atoms. The Cs atoms occupy the corners with a 1a Wyckoff site and fractional coordinates (0, 0, 0); Pb occupies the body-centered position with a 1b Wyckoff site and fractional coordinates (0.5, 0.5, 0.5); and Br is located at the face center with a 3c Wyckoff position and fractional coordinates (0, 0.5, 0.5). The $2 \times 2 \times 2$ supercell of the $CsPbBr_3$ crystal is illustrated in Fig. 1(b), where the transition metal element Cu replaces the Pb atoms in the supercell, with concentrations (x) of 0, 12.5%, 25%, 50%, 75%, and 100%. The evaluated parameters for unalloyed and Pb-Cu alloyed halide perovskites are presented in Table 1 and compared with previous studies.
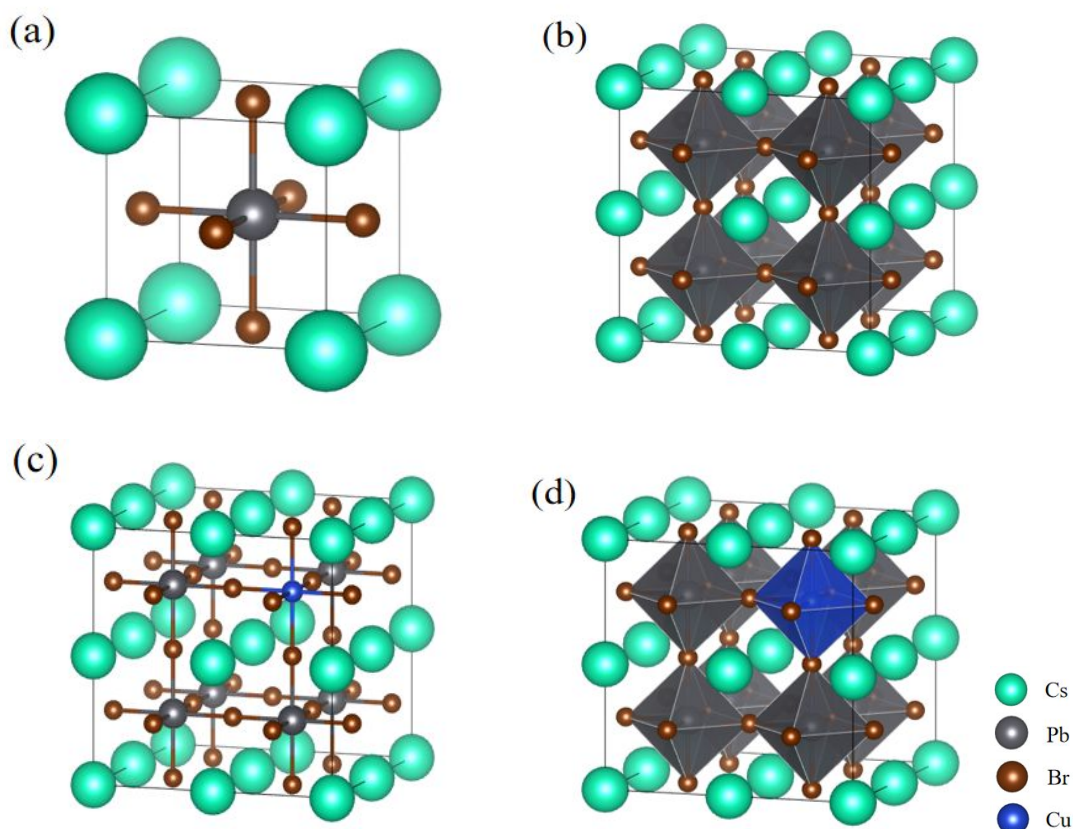


**Fig. 1** The primitive cell of (a) $CsPbBr_3$ (balk-and-stick), $2 \times 2 \times 2$ supercell structures of (b) $CsPbBr_3$ (polyhedral), (c) $CsPb_{0.875}Cu_{0.125}Br_3$ (balk-and-stick), and (d) $CsPb_{0.875}Cu_{0.125}Br_3$ (polyhedral).

Studies have shown that the stability of the $BX_6$ octahedral framework is a fundamental prerequisite for determining the overall stability of perovskites[45]. Theoretically, the crystallographic stability of the perovskite can be estimated using the tolerance factor ($t$) [47], defined as Eq. (1).

$$t = (R_A + R_X)/\sqrt{2}(R_B + R_X) \qquad (1)$$

where $R_A$, $R_B$, and $R_X$ respectively represent the radii of A-site cations, B-site cations, and X-site anions. Shanon-Prewitt effective ionic radii were used to calculate the tolerance factor of the materials[48-49]. In this study, the optimized lattice constant for the pure $CsPbBr_3$ crystal unit cell is determined to be 5.99 Å, which aligns with experimental results[43] and computational findings[50], indicating the reasonability of the computational model. Due to the GGA-PBE method's tendency to overestimate lattice constants, the lattice constants calculated in this study are slightly larger than the experimental values. The computational results (Table 1) reveal that with the introduction of Cu, the lattice constants of the alloyed systems gradually decrease. This reduction is attributed to the smaller effective ionic radius of Cu (0.73 pm) compared to Pb (1.19 pm), leading to lattice contraction. Typically, when the $t$ falls within the range of 0.813 to 1.107[51], the crystal structure of the material is considered sTable. Tolerance factor calculations in Table 1 demonstrate that both the pure $CsPbBr_3$ and alloyed $CsPb_{1-x}Cu_xBr_3$ crystal structures are sTable.

Moreover, the formation enthalpy ($E_f$) are calculated, using the following equations, to confirming their thermodynamic stability[5252].

For an unalloyed system,

$$E_f(CsPbBr_3) = \frac{[E_{tot}(CsPbBr_3) - E(Cs) - E(Pb) - 3E(Br)]}{N} \qquad (2)$$

For a alloyed system,

$$E_f(CsPb_{1-x}Cu_xBr_3) = \frac{[E_{tot}(CsPb_{1-x}Cu_xBr_3) - E(Cs) - (1-x)E(Pb) - xE(Cu) - 3E(Br)]}{N} \qquad (3)$$

where $E(Cs)$, $E(Pb)$, $E(Cu)$, and $E(Br)$ are the energy of Cs, Pb, Cu, and Br atoms, respectively, whereas $E_{tot}(CsPb_{1-x}Cu_xBr_3)$ represents the unit cell total energy of $CsPb_{1-x}Cu_xBr_3$ and N is the number of atoms in the unit cell. The stability of the crystal structure can be assessed by the formation enthalpy per unit atom, and a negative formation enthalpy indicates the thermodynamic stability of the material. The calculated formation enthalpy are also listed in Table 1, and both pure $CsPbBr_3$ and alloyed $CsPb_{1-x}Cu_xBr_3$ exhibit negative binding energies, indicating their thermodynamic stability, although the numerical value of the $E_f$ increases slightly as

the Cu concentration increases.

**Table 1** Lattice constants *a*, Tolerance factor *t* and formation enthalpy $E_f$ for $CsPb_{1-x}Cu_xBr_3$ structures.

| Phase | $a/Å$ | $t$ | $E_f$ | Reference |
|-------|-------|-----|-------|-----------|
| $CsPbBr_3$ | 5.98/5.94 | — | — | Cal.[43]/Exp.[50] |
| $CsPbBr_3$ | 5.99 | 0.815 | -1.73 | This work |
| Pb7Cu1 | 5.90 | 0.830 | -1.66 | This work |
| Pb6Cu2 | 5.81 | 0.846 | -1.59 | This work |
| Pb4Cu4 | 5.58 | 0.879 | -1.46 | This work |
| Pb2Cu6 | 5.44 | 0.915 | -1.36 | This work |
| $CsCuBr_3$ | 5.27 | 0.954 | -1.26 | This work |

## 3.2. Electronic properties

### 3.2.1. Band Structure

In this section, to understand the electronic behavior of cubic $CsPbBr_3$ and its Cu-alloyed counterparts, we calculated their band structures, density of states (DOS) and crystal orbital Hamilton population (COHP). The band structure calculation results for PBE and PBE+SOC are respectively shown in Fig. 2 and Fig. 3, with the Fermi level set to 0 eV for ease of discussion as indicated by the red dashed line. Fig. 2(a) presents the band structure of pure $CsPbBr_3$ perovskite, calculated using the PBE. The valence band maximum and conduction band minimum both occur at the R-point, indicating a direct bandgap semiconductor with a bandgap value of 1.769 eV, which aligns well with other computational results[43]. Due to the limitations of the PBE method, the calculated bandgap is often lower than the experimental value. However, our focus in this work is on the variation trend of the bandgap by Cu-alloying, disregarding the associated gap errors introduced by PBE method. When considering the SOC effect, the bandgap of pure $CsPbBr_3$ is 0.679 eV, as shown in Fig. 3(a). Compared to without SOC, the inclusion of SOC significantly reduces the bandgap value, with no apparent changes in the valence band structure, while the degeneracy phenomenon of the energy valley at the bottom of the conduction band disappears. As shown in Fig. 2(b)-(f) and 3(b)-(f), for the Cu-alloyed systems, regardless of whether SOC is considered, both the conduction band minimum and valence band maximum shift to higher energies. Additionally, the Cu-alloyed systems exhibit characteristics

of p-type degenerate semiconductors. This is because when impurities are introduced into semiconductors through doping or alloying at low impurity concentrations, discrete impurity energy levels are generated in the bandgap. With increasing impurity concentration, impurity atoms interact with each other, causing the impurity energy levels to split into bands. For the lead-copper alloying system in this study, the introduction of a high concentration of Cu atoms widens and extends the acceptor band near the valence band, which become part of the valence band, thus resulting in the formation of a p-type degenerate semiconductor. In a p-type degenerate semiconductor, the Fermi level is situated within the valence band. This phenomenon is known as the Moss–Burstein effect. Additionally, the minimum of the conduction band and the maximum of the valence band in the Cu-alloyed systems do not coincide, indicating that they are indirect bandgap semiconductors. However, the situation appears to be different when considering SOC. For $CsPb_{0.875}Cu_{0.125}Br_3$ and $CsPb_{0.75}Cu_{0.25}Br_3$, both the CBM and VBM occur at the G-point, indicating that they are direct bandgap semiconductors. Additionally, for $CsPb_{0.25}Cu_{0.75}Br_3$, the CBM appears at the R-point, rather than the M-point as calculated by PBE. Compared to indirect bandgap semiconductors, direct bandgap semiconductors are generally more conducive to light absorption, making them promising materials for light absorber layer in solar cells. The bandgap of a semiconductor is defined as the energy difference between the conduction band minimum and the valence band maximum. Table 2 presents the calculated bandgap values for unalloyed and Cu-alloyed systems in this study, comparing them with other computational results or experimental values. It can be observed that the bandgap values of the alloyed systems are dependent on the concentration of Cu. Except for the $CsPb_{0.50}Cu_{0.50}Br_3$ sample, as the Cu concentration increases, the bandgap tends to increase whether with or without SOC. Since SOC effects do not exist in $CsCuBr_3$, the band structures calculated by both methods show no significant differences. Additionally, for Pb-contained compounds, the bandgap values tend to decrease when SOC is included compared to when SOC is not included.
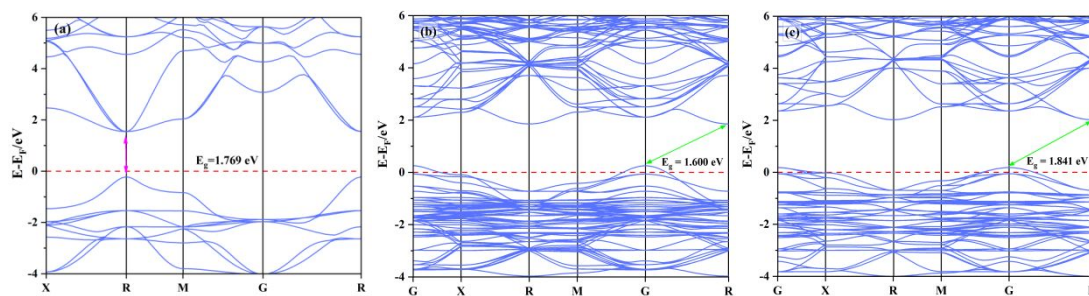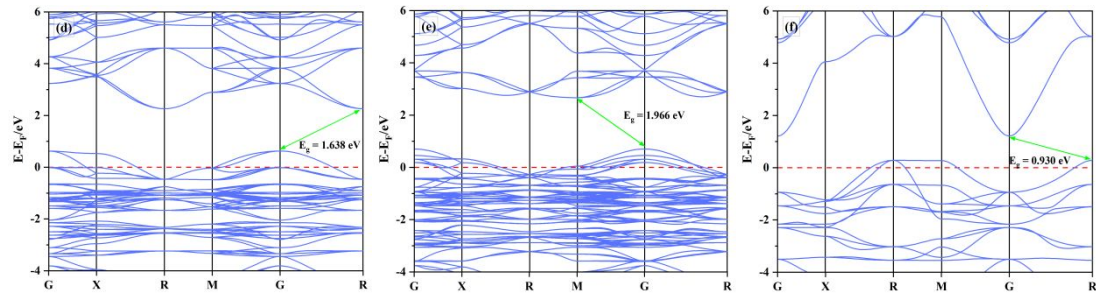
**Fig. 2** The band structures of (a) CsPbBr$_3$, (b) CsPb$_{0.875}$Cu$_{0.125}$Br$_3$, (c) CsPb$_{0.75}$Cu$_{0.25}$Br$_3$, (d) CsPb$_{0.5}$Cu$_{0.5}$Br$_3$, (e) CsPb$_{0.25}$Cu$_{0.75}$Br$_3$, and (f) CsCuBr$_3$ by PBE functional, respectively.
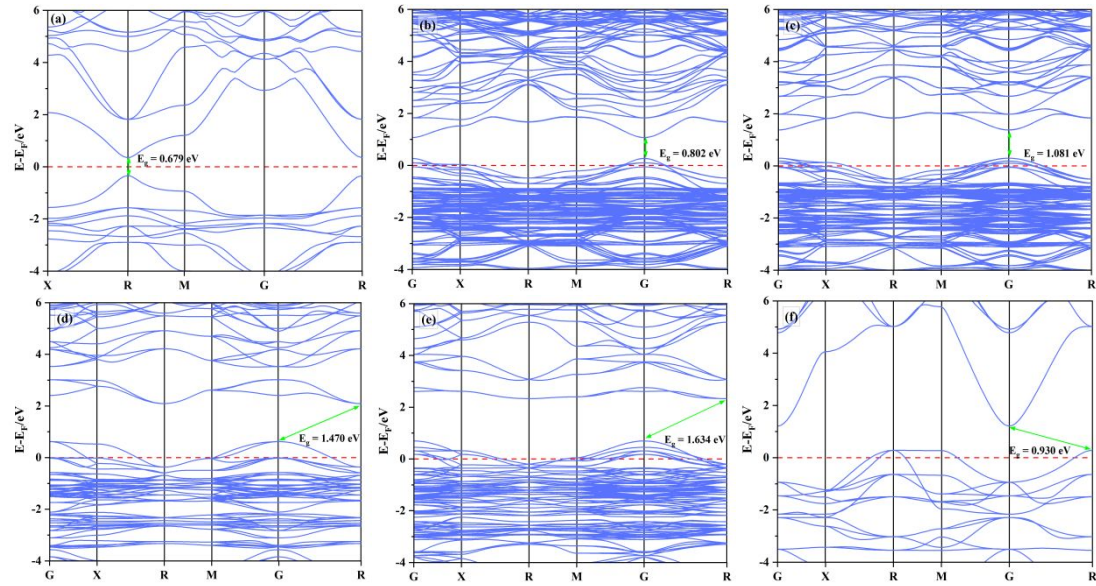


**Fig. 3** The band structures of (a) CsPbBr$_3$, (b) CsPb$_{0.875}$Cu$_{0.125}$Br$_3$, (c) CsPb$_{0.75}$Cu$_{0.25}$Br$_3$, (d) CsPb$_{0.5}$Cu$_{0.5}$Br$_3$, (e) CsPb$_{0.25}$Cu$_{0.75}$Br$_3$, and (f) CsCuBr$_3$ by PBE functional with SOC, respectively.

**Table 2** The energy band gaps (E$_g$) of CsPb$_{1-x}$Cu$_x$Br$_3$ (x=0, 0.125, 0.25,0.5, 0.75,1)

| Phase | PBE without SOC | | PBE with SOC | | Reference |
|---|---|---|---|---|---|
| | Band gap | Band type | Band gap | Band type | |
| CsPbBr$_3$ | 1.796[39]/2.32[54] | Direct | — | — | Cal./Exp. |
| CsPbBr$_3$ | 1.769 | Direct | 0.679 | Direct | This work |
| Pb7Cu1 | 1.600 | Indirect | 0.802 | Direct | This work |
| Pb6Cu2 | 1.841 | Indirect | 1.081 | Direct | This work |
| Pb4Cu4 | 1.638 | Indirect | 1.470 | Indirect | This work |
| Pb2Cu6 | 1.966 | Indirect | 1.634 | Indirect | This work |
| CsCuBr$_3$ | 0.930 | Indirect | 0.930 | Indirect | This work |

9

### 3.2.2. Density of States and COHP

The crystal orbital Hamilton population (COHP) can be used to analyze the bonding strength of Pb-Br or Cu-Br, thereby analyzing the stability of octahedra in perovskite structures. The total density of states (TDOS), partial density of states (PDOS) and COHP of pure and Cu-alloyed samples are presented in Fig. 4 (a)-(f). From Fig. 4 (a), it can be observed that the valence band of pure $CsPbBr_3$ is mainly contributed by Pb 6p and Br 4p orbitals, while the conduction band is mainly contributed by Pb 6p and Br 4p orbitals, with Cs atoms making very small contributions to both bands. By combining PDOS and COHP plots, it can be observed that in the energy range of -4~-3 eV, the bonding states of the Pb-Br bond are mainly formed by the interaction of Pb 6p and Br 4p orbitals. In the energy range of -3~0 eV, the antibonding states are primarily formed by the interaction of Pb 6s and Br 4p orbitals. In the case of Cu-alloyed systems, the valence band is mainly composed of Pb 6p, Cu 3d, and Br 4p orbitals, while the conduction band is primarily composed of Pb 6p and Br 4p orbitals. This implies that Cu alloying primarily alters the valence band of $CsPbBr_3$, with a relatively small impact on the conduction band. The total density of states (TDOS) for the Cu-alloyed system is broader than that of the unalloyed system, mainly due to the reduced crystal symmetry after doping, leading to enhanced non-locality of electrons. With Cu alloying, both the valence band maximum and the conduction band minimum shift to higher energy states, consistent with the band structure calculations. Furthermore, a comparison of the total density of states (TDOS) between unalloyed and alloyed systems reveals an additional peak in the alloyed system, which is indicated by arrows in Fig. 4 (b)-(e). Combining this observation with the PDOS graphs, it is evident that this peak is due to the hybridization of Cu 3d orbitals with Br 4p orbitals, forming an impurity band. This impurity band is introduced into the valence band, crossing the Fermi level, consistent with the results of the band structure calculations. By combining PDOS and COHP plots, it can be observed that both the bonding and antibonding states of the Cu-Br bond are mainly formed by the interaction of Cu 3d and Br 4p orbitals. The ICOHP value represents the integral of COHP below the Fermi level and can be used to assess the strength of the bonding. From Fig. 5, it can be seen that the ICOHP value of Cu-alloyed systems is greater than that of the pure sample and increases with the Cu content. This indicates that the addition of Cu enhances the bonding of the Pb-Br bond, making the $[PbBr_6]$ octahedra more stable, and this stability increases with the Cu content. In Cu-alloyed systems, the ICOHP values of the Cu-Br bonds are lower

than those of the Pb-Br bonds, suggesting that the stability of the [PbBr$_6$] octahedra is higher than that of the [CuBr$_6$] octahedra. Similarly, as the Cu content increases, the ICOHP values of the Cu-Br bonds also increase, indicating enhanced stability of the [CuBr$_6$] octahedra. For pure CsCuBr$_3$, its valence band is mainly contributed by the Cu 3d and Br 4p orbitals, with a relatively minor contribution from Cs atoms. The conduction band is primarily contributed by Cs 6s, Cs 5p, and Br 4p orbitals, while Cu atoms contribute almost nothing to the conduction band. Furthermore, the valence band of CsCuBr$_3$ crosses the Fermi level, exhibiting characteristics of a p-type degenerate semiconductor. From Fig. 5, it can be seen that the ICOHP value of the Cu-Br bonds in pure CsCuBr$_3$ is greater than that of the Pb-Br bonds, indicating that the stability of the [CuBr$_6$] octahedra is higher.
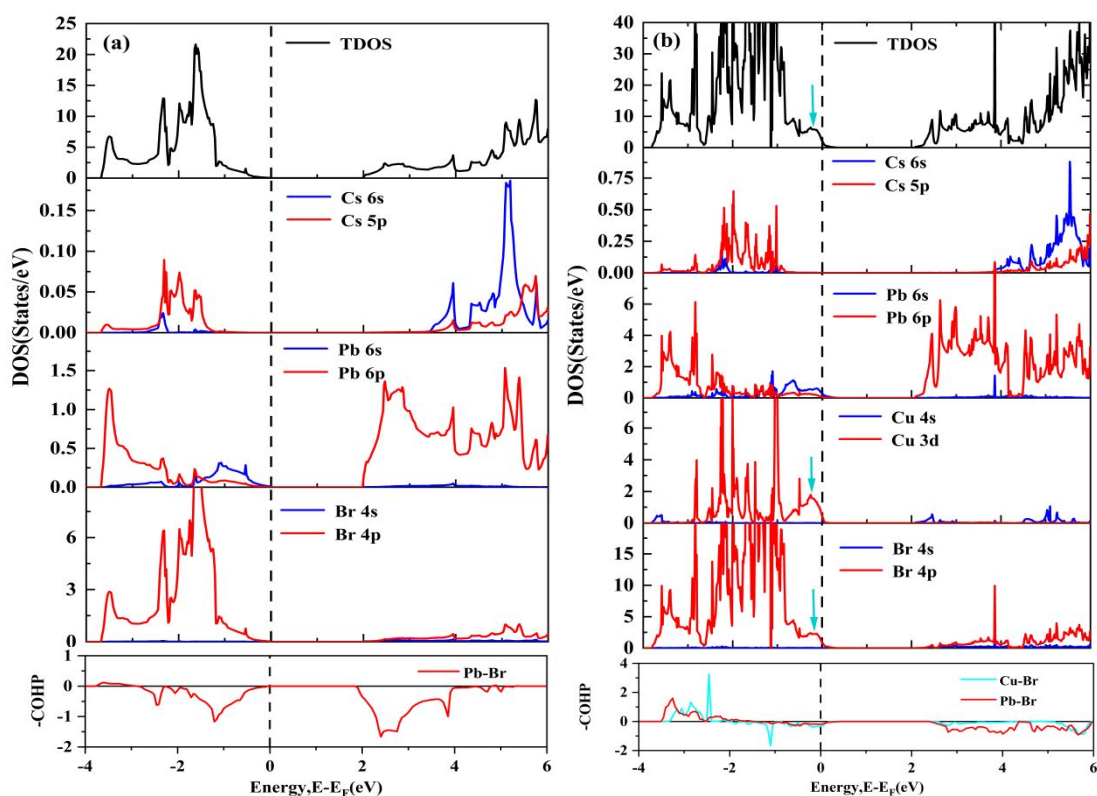
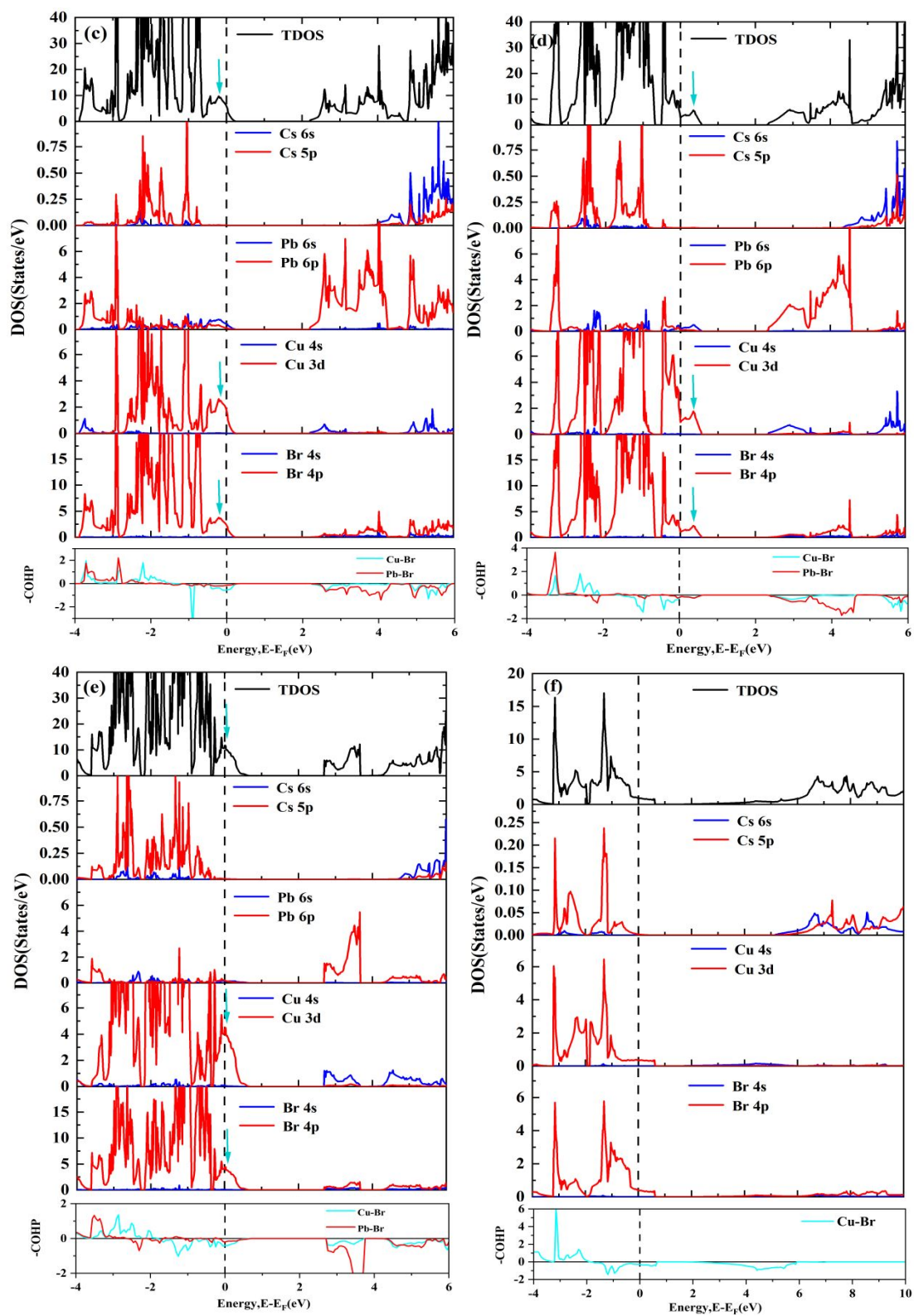**Fig. 4** The DOS and COHP of (a) CsPbBr$_3$ ,(b) CsPb$_{0.875}$Cu$_{0.125}$Br$_3$, (c) CsPb$_{0.75}$Cu$_{0.25}$Br$_3$, (d) CsPb$_{0.5}$Cu$_{0.5}$Br$_3$, (e) CsPb$_{0.25}$Cu$_{0.75}$Br$_3$, and (f) CsCuBr$_3$ by PBE functional, respectively.
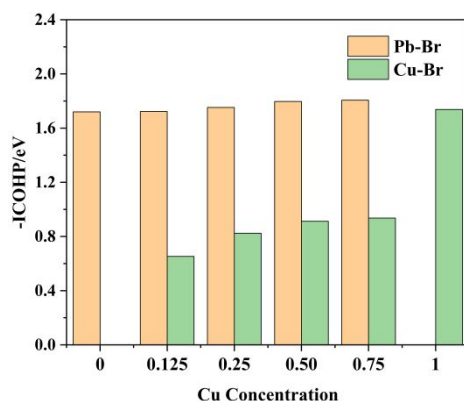
**Fig. 5** Average ICOHP of Pb−Br and Cu−Br Bonds of $CsPb_{1-x}Cu_xBr_3$.

### 3.2.3. Charge density distribution

The bonding characteristics of pure and Cu-alloyed $CsPbBr_3$ were analyzed, as shown in Fig. 6. In Fig. 6(a), it can be observed that there is a high charge density around the Br atoms, indicating ionic bond characteristics. Additionally, there is a small charge density distributed between the Pb and Br atoms, which is a feature of covalent bonding. This indicates that in pure $CsPbBr_3$, the bond between Pb and Br atoms is a mixture of ionic and covalent characteristics. As shown in Fig.6 (b)-(f), for Cu-alloyed and pure $CsCuBr_3$, the presence of Cu 3d electrons results in highly localized charge density around the Cu atoms. Compared to the Pb-Br bonds, the Cu-Br bonds are also a mixture of ionic and covalent characteristics, but they exhibit a stronger ionic bond nature.
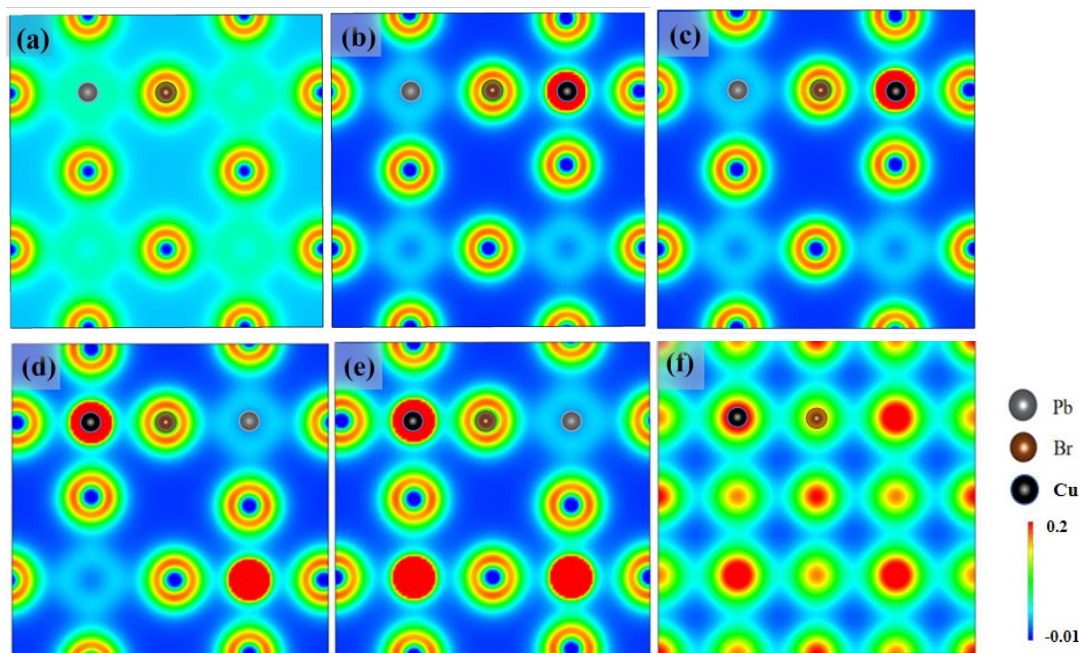


**Fig. 6** Electronic charge densities of the (001) plane of (a) $CsPbBr_3$ ,(b) $CsPb_{0.875}Cu_{0.125}Br_3$, (c) $CsPb_{0.75}Cu_{0.25}Br_3$, (d) $CsPb_{0.5}Cu_{0.5}Br_3$, (e) $CsPb_{0.25}Cu_{0.75}Br_3$, and (f) $CsCuBr_3$ by PBE functional,

respectively.

### 3.2.4. Effective mass

The effective mass summarizes the interaction between the internal potential field within a semiconductor at specific positions in the Brillouin zone and its charge carriers. Generally, the smaller the effective mass, the higher the carrier mobility. The effective mass $m^*$ is defined as[55]:

$$m^* = \hbar^2 \left[ \frac{\partial^2 E(k)}{\partial^2 k} \right]^{-1} \qquad (4)$$

Here, $m^*$ represents the effective mass of electrons/holes, $\hbar$ is the reduced Planck constant, $k$ is the wave vector, and $E(k)$ is the energy of electrons at the wave vector $k$ in the band. In this study, we calculated longitudinal and transversal effective mass of electrons/holes using the band structures fitted with Equation (4) by the PBE and PBE+SOC methods. The results are summarized in Table 3. For CsPbBr$_3$, the transversal hole effective mass obtained with the PBE+SOC method is 0.269, in good agreement with Shi et al.'s findings[43] of 0.267. However, there are slight discrepancies in the calculated electron effective masses. Although both considered SOC effects, Shi et al. employed the HSE functional to calculate the band structure, which differs from the PBE functional used in this study. In PBE calculations for CsPbBr$_3$, the electron effective mass exhibits degeneracy at the CBM, leading to two heavy electrons and one light electron. After considering SOC, the phenomenon of energy valley degeneracy disappears. This change in energy valley degeneracy also occurs in other samples. From this, it can be concluded that the SOC effect significantly impacts the effective mass of charge carriers, thereby influencing the calculation of other carrier properties. Therefore, all subsequent calculations involving the effective mass have taken SOC into account. The DOS effective mass ($m_D^*$) of the valleys can be calculated with the formula[56],

$$m_D^* = S^{2/3} \left( m_l m_t^2 \right)^{1/3} \qquad (5)$$

where S is the energy degeneracy of the valley, and $m_l$, $m_t$ are the longitudinal and the transversal effective mass, respectively. The conductivity effective mass is calculated with the formula[56],

$$\frac{1}{m_\sigma^*} = \frac{1}{3} \left( \frac{1}{m_l} + \frac{2}{m_t} \right) \qquad (6)$$

The calculated effective masses of these valleys are listed in Table 4.

**Table 3** Calculated longitudinal and transversal effective mass values of hole and electron of $CsPb_{1-x}Cu_xBr_3$. L represents light carrier and H represents heavy carrier.

| | PBE without SOC | | | | PBE with SOC | | | |
| | $m_h^*/m_0$ | | $m_e^*/m_0$ | | $m_h^*/m_0$ | | $m_e^*/m_0$ | |
| Phase | $m_l$ | $m_t$ | $m_l$ | $m_t$ | $m_l$ | $m_t$ | $m_l$ | $m_t$ |
|---|---|---|---|---|---|---|---|---|
| $CsPbBr_3$ | — | — | — | — | 0.267[43] | — | 0.301[43] | — |
| $CsPbBr_3$ | 0.255 | 0.255 | 0.115(L) 0.948(H) 0.948(H) | 0.115(L) 0.948(H) 0.948(H) | 0.283 | 0.283 | 0.269 | 0.269 |
| Pb7Cu1 | 0.226 | 0.226 | 0.400 | 0.400 | 0.198 | 0.198 | 0.197 | 0.197 |
| Pb6Cu2 | 0.455 | 0.455 | 0.395 | 0.395 | 0.549 | 0.549 | 0.290 | 0.290 |
| Pb4Cu4 | 0.300(L) 1.272(H) | 0.300(L) 1.272(H) | 0.198 | 0.198 | 0.297(L) 1.297(H) | 0.297(L) 1.297(H) | 0.430 | 0.430 |
| Pb2Cu6 | 0.615 | 0.615 | 0.559 | 0.559 | 0.616 | 0.616 | 1.946 | 1.946 |
| $CsCuBr_3$ | 0.398(L) 66.667(H) | 0.398(L) 66.667(H) | 0.335 | 0.335 | 0.398(L) 66.667(H) | 0.398(L) 66.667(H) | 0.335 | 0.335 |

**Table 4** Calculated DOS and conductivity effective mass values of hole and electron of $CsPb_{1-x}Cu_xBr_3$ with SOC. L represents light carrier and H represents heavy carrier.

| | $m_h^*/m_0$ | | | $m_e^*/m_0$ | | |
| Phase | $S$ | $m_D^*$ | $m_\sigma^*$ | $S$ | $m_D^*$ | $m_\sigma^*$ |
|---|---|---|---|---|---|---|
| $CsPbBr_3$ | 1 | 0.283 | 0.283 | 1 | 0.269 | 0.269 |
| Pb7Cu1 | 1 | 0.198 | 0.198 | 1 | 0.197 | 0.197 |
| Pb6Cu2 | 1 | 0.549 | 0.549 | 1 | 0.290 | 0.290 |
| Pb4Cu4 | 2 | 0.471(L) 2.059(H) | 0.297(L) 1.297(H) | 1 | 0.430 | 0.430 |
| Pb2Cu6 | 1 | 0.616 | 0.616 | 1 | 1.946 | 1.946 |
| $CsCuBr_3$ | 2 | 0.632(L) 105.827(H) | 0.398(L) 66.667(H) | 1 | 0.335 | 0.335 |

## 3.3. Transport properties

### 3.3.1. Carrier concentration

Carrier concentration refers to the number of charge carriers per unit volume. In degenerate semiconductors, the distribution of carriers no longer follows the Boltzmann statistics, and it is necessary to use the Fermi distribution function to analyze the statistical distribution of carriers in the energy bands. In a valley, the number of hole carriers in p-type degenerate semiconductors can be calculated using the following equation[56]:

$$p = 2\left(\frac{2\pi m_D^* K_B T}{h^2}\right)^{3/2} \frac{2}{\sqrt{\pi}} \int_0^\infty \frac{x^{1/2}}{1+\exp{(x-\xi)}} dx = N_V \frac{2}{\sqrt{\pi}} F_{1/2}(\xi) \qquad (7)$$

where $x = \frac{E_v - E}{K_B T}$, $\xi = \frac{E_v - E_F}{K_B T}$, $m_D^*$ represents DOS effective mass, $h$ denotes the Planck constant, $K_B$ represents the Boltzmann constant, $T$ represents the thermodynamic temperature (taken as 300K in this study), $E_F$ represents the Fermi level, and $E_v$ represents the energy of the valence band maximum. The function $F_{1/2}$ ($\xi$) in Equation (7) is referred to as the Fermi function, which cannot be integrated directly and can only be approximated. In this work, we use the fitting formula proposed by Marshak et al.[57] to approximate the Fermi function. In p-type degenerate semiconductors, electrons follow the Boltzmann distribution, and their concentration can be calculated using the following formula:

$$n = 2\left(\frac{2\pi m_D^* K_B T}{h^2}\right)^{3/2} \exp\left[\frac{-\left(E_C - E_F\right)}{K_B T}\right] \qquad (8)$$

The hole and electron concentration values obtained in this work are listed in Table 5. The calculation results indicate that the hole concentration in pure CsPbBr$_3$ is slightly higher than the electron concentration, demonstrating the characteristics of a weak p-type semiconductor. In contrast, the hole concentration in Cu-alloyed and pure CsCuBr$_3$ is significantly higher than the electron concentration, exhibiting the characteristics of a p-type semiconductor.

**Table 5** Calculated values of hole and electron of CsPb$_{1-x}$Cu$_x$Br$_3$ with SOC. L represents light

carrier and H represents heavy carrier.

| Phase | h | | e | |
|---|---|---|---|---|
| | $\dfrac{E_v - E_F}{K_B T}$ | $p*10^{21}$/cm$^{-3}$ | $-\dfrac{E_C - E_F}{K_B T}$ | $n*10^{21}$/cm$^{-3}$ |
| CsPbBr$_3$ | -1.33 | 0.91 | -1.33 | 0.84 |
| Pb7Cu1 | 1.04 | 3.59 | -4.14 | 0.35 |
| Pb6Cu2 | 1.14 | 17.60 | -5.33 | 0.02 |
| Pb4Cu4 | 2.40 | 27.42 | -8.09 | 0.112 |
| Pb2Cu6 | 2.69 | 46.64 | -9.00 | 0.008 |
| CsCuBr$_3$ | 1.09 | 21.05 | -4.68 | 0.045 |

### 3.3.2. Carrier mobility

Based on the effective mass, this study investigates the carrier mobility using the deformation potential theory. For three-dimensional materials, the calculation formula for mobility $\mu$ is as follows:[58]:

$$\mu_\alpha^{3D} = \frac{2\sqrt{2\pi} e C_\alpha^{3D} \hbar^4}{3\left(K_B T\right)^{3/2} E_\alpha^2 \left(m_D^*\right)^{3/2} m_\sigma^*} \tag{9}$$

Where $e$ represents the elementary charge, $\hbar$ denotes the reduced Planck constant, $C_\alpha^{3D}$ represents the elastic constant along the direction of carrier transport, $E_\alpha$ denotes the deformation potential energy. The formula for calculating $C_\alpha^{3D}$ is:

$$C_\alpha^{3D} = \frac{1}{V_0} \frac{\partial^2 E}{\partial\left(\delta l/l_0\right)^2}\bigg|_{l=l_0} \tag{10}$$

Where $V_0$ is the fully optimized cell volume, $E$ is the total energy of the cell, $l_0$ is the lattice constant along the $\alpha$ direction, and $\delta l$ represents the deformation parameter along the $l$ direction. In this study, deformation parameters of -1.0%, -0.5%, 0%, 0.5%, and 1.0% were employed. To ensure accuracy, we considered the Poisson effect when applying deformation to the materials. Therefore, when the lattice is stretched in one direction and relaxed, we fixed the stretching direction while allowing the remaining directions to move freely to obtain a more reasonable structure with the lowest energy. The calculation method for $E_\alpha$ is as follows:

$$E_\alpha = \frac{\partial\left(E_{edge} - E_{ref}\right)}{\partial\left(\delta l/l_0\right)} \tag{11}$$

Where $E_{edge}$ is the energy value of the VBM or CBM after lattice deformation, $E_{ref}$ serving as the reference level, set to the average value of the first valence

17

band[59]. According to Equations (9)-(11) and the effective masses calculated earlier, this study computed the elastic constants, deformation potentials, and carrier mobilities. The results are listed in Table 6. In the fittings conducted in this article, the fitting parameter $R^2$ is all greater than 0.90. The deformation potentials of the CBM and VBM of pure $CsPbBr_3$ and Cu-alloyed $CsPbBr_3$ are not equal. Upon observation of the carrier calculation formulas, the mobility is mainly determined by three variables. Under different structures, there are only minor differences between the elastic constants and deformation potential, indicating that these two parameters are not the determining factors affecting mobility. On the other hand, there are significant differences in the effective hole mass among different structures and directions, reflected in the formula as the power exponent of the effective mass being 2.5. Therefore, the effective mass is the primary factor influencing the final results. When valley degeneracy occurs, each valley contributes to the carrier mobility. The mobility of multi-valley carriers, denoted as $\mu_{mv}$, can be calculated using the following equation[56]:

$$\mu_{mv} = \sum_j \frac{q_j}{q} \mu_{svj} \tag{12}$$

where j is the j-th valley and $q = \sum_j q_j$ is the total carrier quantity of all valleys. Since the energy of each valley is equal, the difference between the Fermi level and the energy of each valley is also equal. Therefore, combining equations (11) and (12), the expression for the mobility of multi-valley carriers can be simplified to:

$$\mu_{mv} = \sum_j \frac{m_j^{*3/2}}{M^*} \mu_{svj} \tag{13}$$

where $M^* = \sum_j m_j^{*3/2}$, $m_j^{*3/2}$ is the 3/2 power of the effective mass of the j-th valley.

The calculation results of multi-valley carrier mobility are shown in Table 6 and Fig. 7. Some studies[60] have reported electron and hole mobilities of $CsPbBr_3$ to be 679 $cm^2$ $V^{-1}$ $s^{-1}$ and 52 $cm^2$ $V^{-1}$ $s^{-1}$, respectively. While the electron mobility matches well with the results obtained after considering SOC in this study, there is a significant discrepancy in hole mobility. Other research[61] indicates that the experimental hole concentration of $CsPbBr_3$ single crystal samples typically falls within a wide range, approximately 10-1000 $cm^2$ $V^{-1}$ $s^{-1}$. The significant discrepancies in reported carrier mobilities across various literature are mainly due to: 1) the presence of defects in experimental materials, while the computed structures are considered ideal models;

and 2) differences in the methods used for computation, which can lead to deviations in results. Regarding the deformation potential theory employed in this study, it does not account for factors such as lattice vibrations and interactions between electrons, resulting in certain errors in the calculated results. In Fig. 7, with SOC considered, only $CsPb_{0.25}Cu_{0.75}Br_3$ shows higher average hole mobility than electron mobility, confirming its p-type semiconductor behavior. Furthermore, $CsPb_{0.875}Cu_{0.125}Br_3$ demonstrates significantly enhanced hole and electron mobilities, beneficial for efficient carrier transport and collection, making it a promising candidate for the absorber layer in solar cells. However, electron and hole mobilities of other Cu-alloyed compounds are reduced compared to pure $CsPbBr_3$, leading to diminished carrier transport performance.

**Table 6** Calculated single-valley carrier mobility ($\mu_{sv}$) and many-valley carrier mobility ($\mu_{mv}$) of $CsPb_{1-x}Cu_xBr_3$ by using PBE + SOC at 300 K. Where e represents electron and h represents hole, L represents light carrier and H represents heavy carrier.

| Phase | Carrier Type | $C_\alpha$ /GPa | $E_\alpha$ /eV | $\mu_{sv}$ /cm$^2$ V$^{-1}$ s$^{-1}$ | $q_j$ /q | $\mu_{mv}$ /cm$^2$ V$^{-1}$ s$^{-1}$ |
|---|---|---|---|---|---|---|
| CsPbBr$_3$ | h | 41.28 | -10.44 | 543.82 | 1 | 543.82 |
| | e | 41.28 | -8.74 | 880.76 | 1 | 880.76 |
| Pb7Cu1 | h | 30.18 | -6.86 | 2250.77 | 1 | 2250.77 |
| | e | 30.18 | -5.76 | 3233.19 | 1 | 3192.53 |
| Pb6Cu2 | h | 21.51 | -5.16 | 217.75 | 1 | 217.75 |
| | e | 21.51 | -4.41 | 1469.96 | 1 | 1469.96 |
| Pb4Cu4 | h | 15.49 | -5.35 | 345.08 (L) | 0.186 | 94.91 |
| | | | | 37.75 (H) | 0.814 | |
| | e | 15.49 | -3.87 | 522.19 | 1 | 522.19 |
| Pb2Cu6 | h | 28.88 | -5.36 | 281.13 | 1 | 281.13 |
| | e | 28.88 | -5.05 | 17.96 | 1 | 17.96 |
| CsCuBr$_3$ | h | 30.16 | -5.42 | 314.30 (L) | 0.0059 | 1.86 |
| | | | | 0.00087 (H) | 0.9941 | |
| | e | 30.16 | -5.35 | 993.07 | 1 | 993.07 |
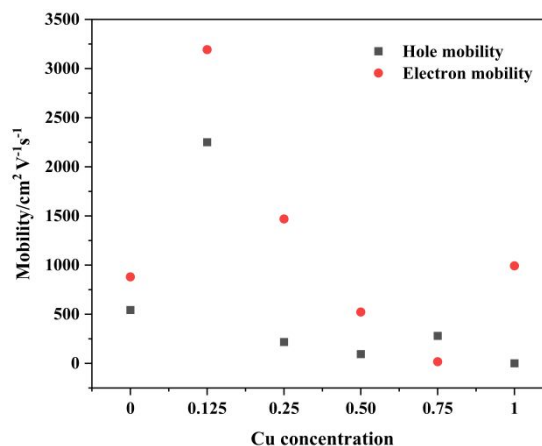
**Fig. 7** Calculated average carrier mobility ($\mu_{avg}$) of $CsPb_{1-x}Cu_xBr_3$ by (a) PBE + SOC at 300 K.

## 3.4. Optical properties

In this section, we simulated the dielectric function ($\varepsilon$), optical absorption coefficient ($\alpha$), and reflectivity ($R$) for pristine $CsPbBr_3$ and Cu-alloyed $CsPb_{1-x}Cu_xBr_3$ samples. These optical properties are closely related to the complex dielectric function, which can be expressed using the following formula[62]:

$$\varepsilon(\omega) = \varepsilon_1(\omega) + i\varepsilon_2(\omega) \tag{14}$$

Here, $\varepsilon_1(\omega)$ and $\varepsilon_2(\omega)$ represent the real and imaginary parts of the dielectric function, respectively. The other well-known formula for optical properties such as absorption $\alpha(\omega)$ and reflectivity $R(\omega)$ is defined as follows in Equations (15)–(16):

$$\alpha(\omega) = \sqrt{2}\omega\left[\sqrt{\varepsilon_1(\omega)^2 + \varepsilon_2(\omega)^2} - \varepsilon_1(\omega)\right]^{1/2} \tag{15}$$

$$R(\omega) = \left|\frac{1 - \sqrt{\varepsilon(\omega)}}{1 + \varepsilon(\omega)}\right|^2 \tag{16}$$

The dielectric function is used to describe the behavior of materials under incident light. Other spectroscopic information can be obtained through the dielectric function. Fig. 8(a) and 8(c) show the real and imaginary parts of the dielectric function for pure $CsPbBr_3$ and Cu-alloyed materials. The real part $\varepsilon_1$ of the dielectric function at 0 eV is called the dielectric constant $\varepsilon_0$. The dielectric constant regulates the charge recombination rate and energy harvesting efficiency of optoelectronic devices. A higher $\varepsilon_0$ value indicates lower charge recombination rates and higher efficiency of optoelectronic devices[63]. As seen in Fig. 8(a) and 8(b), compared to unalloyed $CsPbBr_3$, Cu-alloyed systems and pure $CsCuBr_3$ have a larger dielectric constant, which increases with the increase of Cu content, indicating that Cu-alloyed

20

materials have a lower carrier recombination rate and are suiTable for optoelectronic device applications. The imaginary part of the dielectric function $\varepsilon_2$ is associated with interband transitions of excited electrons[65] and closely related to the optical absorption properties. From Fig. 8(c), pure $CsPbBr_3$ exhibits four significant peaks in $\varepsilon_2$. When the photon energy is below the semiconductor's bandgap width of 1.769 eV, the $\varepsilon_2$ value remains relatively low. At this stage, $CsPbBr_3$ mainly absorbs weakly, relying on free carriers within the energy band, with no carrier transitions occurring. However, as the energy surpasses 1.769 eV, $\varepsilon_2$ sharply rises, peaking around 3.90 eV. This shift primarily results from intrinsic absorption within $CsPbBr_3$, where valence band electrons are excited to the conduction band, generating electron-hole pairs through interband transitions. As our study focuses solely on the optical behavior of materials within the solar photon energy range (0.5-4.1 eV, 300~2500 nm), the discussion excludes the other three peaks of $\varepsilon_2$, corresponding to photon energies beyond this scope. The significant differences in the imaginary part of the dielectric function between unalloyed and Cu-alloyed $CsPbBr_3$ samples mainly manifest in the low-energy region. Compared to the pure $CsPbBr_3$ sample, Cu-alloyed systems and pure $CsCuBr_3$ exhibit a significant peak in $\varepsilon_2$ in the low-energy region (< 1 eV). As previously mentioned, the Cu-alloyed systems all generate acceptor energy bands, causing the Fermi level to shift towards the valence band. This movement of the Fermi surface allows free carriers with energies lower than the Fermi level to enter the valence band with only a small amount of photon energy absorption. Therefore, these additional peaks mainly arise from electron intra-band transitions within the acceptor bands[66]. When the photon energy exceeds the bandgap values of the Cu-alloyed systems, the value of $\varepsilon_2$ begins to increase, reaching maximum values within the range of 3.5-4.1 eV. During this process, the material undergoes intrinsic absorption, primarily originating from interband transitions of electrons from VBM (Cu 3d and Br 4p orbitals) to CBM (Pb 6p orbitals). For Cu-alloyed $CsPbBr_3$, light absorption begins at very low energy levels.

The absorption coefficient ($\alpha$) is a crucial parameter for evaluating a material's ability to absorb incident photons in photovoltaic devices, such as solar cells, directly impacting the material's photoconversion efficiency. Reflectivity refers to the reflection of light by the material in comparison to the incident light. In general, lower reflectivity indicates higher absorption coefficients and, consequently, higher conversion efficiency for a material[67]. The calculated absorption spectra and reflectance spectra of unalloyed and Cu-alloyed materials are shown in Fig. 8(d) and

8(e). From Fig. 8(d), it can be observed that compared to unalloyed $CsPbBr_3$, Cu-alloyed materials exhibit extra absorption peaks in the low-energy region (< 1.5 eV), consistent with the analysis results of the imaginary part of the dielectric function. For $CsPb_{0.875}Cu_{0.125}Br_3$ and $CsPb_{0.75}Cu_{0.25}Br_3$, their absorption peaks are relatively small when photon energy ranges from 0.5 eV to their bandgap values, resulting in minimal carrier absorption. However, from the bandgap value to 4.1 eV, their intrinsic absorption peaks are similar to pure $CsPbBr_3$, with low reflectivity, enhancing photoelectric conversion efficiency. Additionally, their high dielectric constants suggest lower carrier recombination rates, indicating stronger optical performance within the solar spectrum range compared to pure $CsPbBr_3$, making them potential alternatives for the absorber layer in perovskite solar cells. As for $CsPb_{0.75}Cu_{0.25}Br_3$ and $CsCuBr_3$, significant absorption peaks occur within the energy range from 0.5 eV to the bandgap value due to intraband transitions. However, beyond the bandgap value, their absorption peaks decrease, especially for $CsCuBr_3$, indicating reduced light absorption. Their dielectric constants also suggest lower carrier recombination rates, making them potential candidates for the HTL in solar cells. For $CsPb_{0.5}Cu_{0.5}Br_3$, its intrinsic absorption peak decreases compared to pure $CsPbBr_3$, but still exhibits some absorption ability, resulting in lower transparency to solar photons. Therefore, it is not suiTable as an HTL material for solar cells.
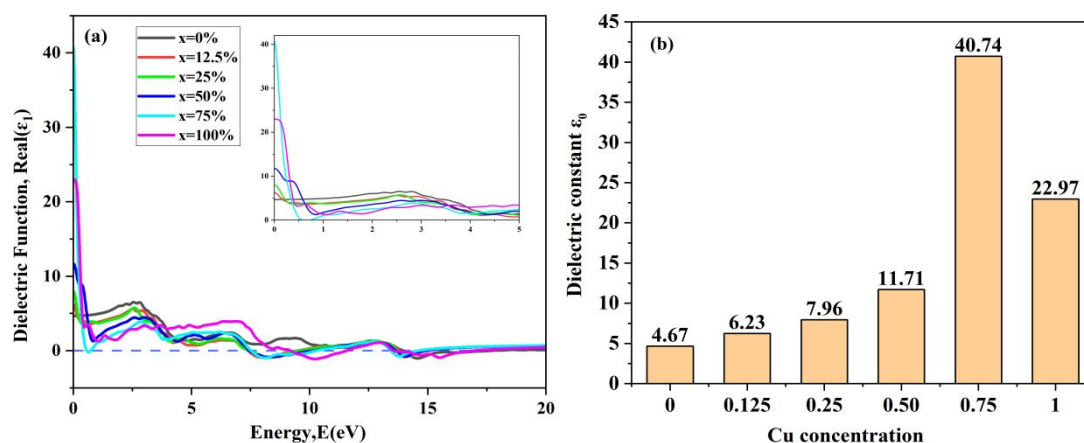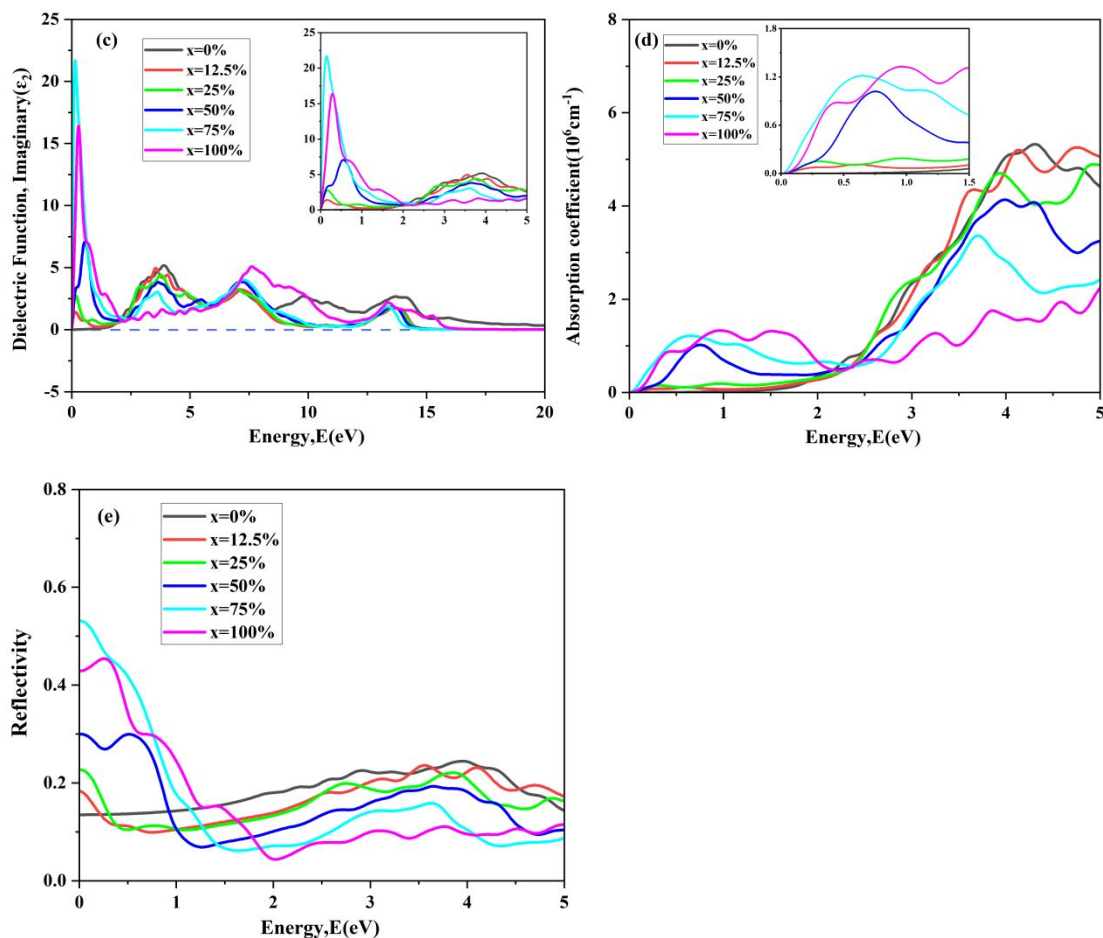
**Fig. 8** The simulated optical properties (a) real part $\varepsilon_1$ of dielectric functionand, (b) dielectric constant $\varepsilon_0$, (c) imaginary part $\varepsilon_2$ of dielectric function, (d) absorption coefficient, and (d) reflectivity of $CsPb_{1-x}Cu_xBr_3$ (x=0, 0.125, 0.25, 0.5, 0.75,1).

## 4. Conclusion

In this work, we utilized first-principles DFT calculations to predict the crystal structure, mechanical, optoelectronic, and carrier transport properties of the new alloyed 3D $CsPb_{1-x}Cu_xBr_3$ (x = 0, 0.125, 0.25, 0.5, 0.75, 1) CHPs. Our calculations revealed that the increasing Cu(II) concentration results in a gradual reduction of the lattice of host $CsPbBr_3$ thanks to its smaller effective ionic radius. The electronic structure simulations showed that Cu 3d orbitals introduced new acceptor bands into the host semiconductor, leading to the p-type degenerate behavior in the band structure of alloyed CHPs. The calculation of COHP shows that the introduction of Cu(II) enhances the stability of [PbBr$_6$] octahedra, which increases with increasing Cu concentration. With the inclusion of spin-orbit coupling effects, the bandgap of the alloyed systems decreased with increasing Cu content, demonstrating tunability of the bandgap. Transport property calculations revealed that SOC significantly influenced

the effective mass of carriers, thereby affecting carrier mobility calculations. When with SOC included, $CsPb_{0.25}Cu_{0.75}Br_3$ maintained p-type behavior. Compared to pure $CsPbBr_3$, $CsPb_{0.875}Cu_{0.125}Br_3$ exhibited higher hole/electron carrier mobility. Optical property calculations showed that $CsPb_{0.75}Cu_{0.25}Br_3$ and $CsCuBr_3$ exhibited lower absorption of solar photons above the bandgap value, indicating higher transparency within this energy range and suggesting their suitability for HTL fabrication in PSCs. Conversely, $CsPb_{0.875}Cu_{0.125}Br_3$ and $CsPb_{0.75}Cu_{0.25}Br_3$ demonstrated stronger light absorption performance than pure $CsPbBr_3$. In view of the above, our comprehensive analysis predicts that $CsPb_{0.875}Cu_{0.125}Br_3$ is a direct bandgap semiconductor with high carrier mobility and strong light absorption, making it a promising candidate for the absorber layer in perovskite solar cells. $CsPb_{0.25}Cu_{0.75}Br_3$, on the other hand, is an indirect bandgap semiconductor with significantly higher hole mobility than electron mobility, and high transparency to solar photons, suggesting its potential application as HTL to enhance the carrier transport and collection efficiency in PSCs.

## Acknowledgments

## References

1.  W. Zhang, G. E. Eperon and H. J. Snaith, *Nat. Energy,* 2016, **1**, 16048.

2.  W. J. Yin, T. Shi and Y. Yan, *Adv. Mater.,* 2014, **26**, 4653-4658.

3.  Q. A. Akkerman, M. Gandini, D. F. Stasio, P. Rastogi, F. Palazon, G. Bertoni, J. M. Ball, M. Prato, A. Petrozza and L. Manna, *Nat Energy,* 2017, **2**, 16194.

4.  K. P. Marshall, M. Walker, R. I. Walton and R. A. Hatton, *Nat. Energy,* 2016, **1**, 16178.

5.  A. Swarnkar, A. R. Marshall, E. M. Sanehira, B. D. Chernomordik, D. T. Moore, J. A. Christians, T. Chakrabarti and J. M. Luther, *Science,* 2016, **354**, 92-95.

6.  G. E. Eperon, G. M. Paterno, R. J. Sutton, A. Zampetti, A. A. Haghighirad, F. Cacialli and H. J. Snaith, *J. Mater. Chem. A,* 2015, **3**, 19688-19695.

7.  T. Krishnamoorthy, H. Ding, C. Yan, W. L. Leong, T. Baikie, Z. Z. Zhang, M. Sherburne, S. Z. Li, M. Asta, N. Mathews and S. G. Mhaisalkar, *Mater. Chem. A,* 2015, **3**, 23829-23832.

8.  D. Yang, M. H. Cao, Q. X. Zhong, P. L. Li, X. H. Zhang and Q. Zhang, *Journal of Materials*

*Chemistry C.,* 2019, **7(4)**, 757-89.

9.  Z. Y. Liu, J. J. Chang, Z. H. Lin, L. Zhou, Z. Yang, D. Z. Chen, C. F. Zhang, S. Z. F. Liu and Y. Hao, Adv. *Energy Mater.,* 2018, **8**, 1703432.

10. Z. Liang, Y. Zhang, H. F. Xu, W. J. Chen, B. Y. Liu, J. Y. Zhang, H. Zhang, Z. H. Wang and D. Kang, *Nature,* 2023, **624**, 557-563.

11. M. Saliba, S. Orlandi, T. Matsui, S. Aghazada, M. Cavazzini, J. Correa-Baena and P. Gao, *Nature energy,* 2016, **1(2)**, 1-7.

12. M. C. Yen, C. J. Lee, K. H. Liu, Y. Peng, J. F. Leng, T. H. Chang, C. C. Chang, K. Tamada and Y. J. Lee, *Nat Commun.,* 2021, **12**, 4460.

13. X. Y. Huang, H. B. Li, C. F. Zhang, S. J. Tan, Z. Z. Chen, L. Chen, Z. D. Lu, X. Y. Wang and M. Xiao, *Nat Commun.,* 2019, **10**, 1163.

14. Q. G. Zhang, B. Wang, W. L. Zheng, L. Kong, Q. Wan, C. Y. Zhang, Z. C. Li, X. Y. Cao, M. M. Liu and L. Li, *Nat Commun.,* 2020, **11**, 31.

15. M. W. Swift and J. L. Lyons, *Journal of Materials Chemistry A.,* 2021, **9(12)**, 7491-5.

16. Y. H. He, L. Matei, H. J. Jung, K. M. McCall, M. Chen, C. C. Stoumpos, Z. F. Liu, J. A. Peters and D. Y. Chung, *Nat. Commun.,* 2018, **9**, 1609.

17. J. T Mulder, I. Fossé, M. A. Jazi, L. Manna and A. J Houtepen, *ACS Energy Lett.,* 2021, **6**, 2519‒2525.

18. S. Heo, K. Roh, F. Y. Zhang, S. E. Tignor, A. B. Bocarsly, A. Kahn and B. P. Rand, *ACS Energy Lett.,* 2022, **7**, 211‒216.

19. K. Ahmad and S. M., *Mobin Energy Technology,* 2020, 1901185.

20. S. Kahmann, O. Nazarenko, S. Y. Shao, O. Hordiichuk, M. Kepenekian, J. Even, M. V. Kovalenko, G. R. Blake and M. A. Loi, *ACS Energy Letters,* 2020, **5(8)**, 2512-2519.

21. T. Krishnamoorthy, H. Ding, C. Yan, W. L. Leong, T. Baikie, Z. Y. Zhang, M. Sherburne, S. Z. Li, M. Asta, N. Mathews and S. G. Mhaisalkar, *Journal of Materials Chemistry A.,* 2015, **3(47)**, 23829-23832.

22. A. J. Lehner , D. H. Fabini, H. A. Evans, C. Hébert, S. R. Smock, J. Hu, H. B. Wang, J. W. Zwanziger, M. L. Chabinyc and R. Seshadri, *Chemistry of Materials,* 2015, **27(20)**, 7137-7148.

23. P. G. Han and K. L.Han, *Energy & Fuels,* 2021, **35(23)**, 18871-18887.

24. B. Saparov, F. Hong, J. Sun, H. Duan, W. W. Meng, S. Cameron, I. G. Hill, Y. Yan and D. B. Mitzi, *Chemistry of Materials,* 2015, **27(16)**, 5622-5632.

25. T. Jun, K. Sim, S. Iimura, M. Sasase, H. Kamioka, J. Kim and H. Hosono, *Adv Mater.,* 2018, **30(43)**, e1804547.

26. P. Ran, L. R. Yang, T. M. Jiang, X. H. Xu, J. Hui, Y. R. Su, C. F. Kuang and X. Liu, Y.

M.Yang, *Advanced Materials*, 2022, **34(42)**, e2205458- e2205458.

27.   F. Zhang, D. W. Yang, Z. F. Shi, C. C. Qin, M. H. Cui, Z. Z. Ma, L. T. Wang, M. Wang, X. Z. Ji, X. Chen, D. Wu, X. J. Li, L. J. Zhang and C. X. Shan, *Nano Today,* 2021, **38**.

28.   L. L. Liu, W. J. Li, X. P. Feng, C. J. Guo, H. M. Zhang, H. T. Wei and B. Yang, *Advanced Science*, 2022, **9(15)**, 2103735.

29.   J. L. Feng, J. X. Wang, D. Wang, M. Han, G. S. Qian, F. Wu, Q. Lin and Z. G. Hu, *ACS Applied Electronic Materials,* 2022, **4(1)**, 225-32.

30.   J. F. Qu, S. H. Xu, H. B. Shao, P. F. Xia, C. G. Lu, C. L. Wang and D. Y. Ban, *Journal of Materials Chemistry C.,* 2023, **11(19)**, 6260-75.

31.   Y. Y. Li, Z. C. Zhou, N. Tewari, M. Ng, P. Geng, D. Z. Chen, P. K. Ko, M. Qammar, L. Guo and J. E. Halpert, *Materials Chemistry Frontiers,* 2021, **5(13)**, 4796-820.

32.   C. Abia, C. A. López, J. Gainza, J. E. F. S. Rodrigues, M. T. Fernández-Díaz, E. Céspedes, J. L. Martínez and J. A. Alonso, *CrystEngComm,* 2023, **25(31)**, 4417-26.

33.   R. Roccanova, A. Yangui, H. Nhalil, H. L. Shi, M. H. Du and B. Saparov, *ACS Applied Electronic Materials,* 2019, **1(3)**, 269-74.

34.   Q. Wang, C. Wang, Z. H. Wang, X. L. Sun, M. Nikl, X. P. Yang and Y. T. Wu, *The Journal of Physical Chemistry Letters,* 2022, **13(39)**, 9066-71.

35.   J. X. Chen, X. Y. Liu, Z. Q. Li, F. Cao, X. Lu and X. S. Fang, *Advanced Functional Materials,* 2022, **32(24)**, 2201066.

36.   R. L. Z. Hoye, J. Hidalgo, R. A. Jagt, J.-P. C.-Baena, T. Fix and J. L. M.-Driscoll, *Advanced Energy Materials,* 2021, **12(4)**.

37.   Z. Z. Ma, X. Z. Ji, S. L. Lin, X. Chen, D. Wu, X. J. Li, Y. Zhang, C. X. Shan, Z. F. Shi and X. S. Fang, *Advanced Materials,* 2023, **35(44)**, 2300731.

38.   C. Cetin, P. Chen, M. M. Hao, D. X. He, Y. Bai, M. Q. Lyu, J.-H. Yun and L. Z. Wang, *Advanced Sustainable Systems,* 2018, **2(8-9)**, 1800032.

39.   K. Said and S. Elkhattabi, *Materials Science in Semiconductor Processing,* 2024, **174**, 108242.

40.   M. M. Hasan, A. Kabir and M. Kamruzzaman, *Results in Physics,* 2022, **41**.

41.   M. Cococcioni and S. De Gironcoli, *Phys. Rev. B,* 2005, **71(3)**, 035105.

42.   Md R. Islam, A.S.M. J. Islam, S.K. Mitro, Md R. H. Mojumder, B. K. Moghal, S. Ahmad , S. Roy and Md Z. Islam, *Journal of Physics and Chemistry of Solids,* 2022, **170**, 110919.

43.   H.-Z. Shi, Y. Jing, W.-H. Li, C. Wang, B.-N. Jia and J. Ren. *Journal of Materials Science,* 2022, **57(42)**, 19846-56.

44.   S. J. Wang, W.-B. Xiao and F. Wang, *RSC ADVANCES,* 2020, **10(54)**, 32364-32369.

45.   M. N. Islam, M. A. Hadi and J. Podder, *AIP Advances,* 2019, **9(12)**, 125321-125321.

46. A. Kojima, K. Teshima, Y. Shirai and T. Miyasaka. *Journal of the American Chemical Society,* 2009, **131(17)**, 6050-6051.

47. V. M. Goldschmidt. *Berichte Der Deutschen Chemischen Gesellschaft (A and B Series),* 1927, **60(5)**, 1263-1296.

48. R. D. Shannon and C. T. Prewitt, *Acta Crystallogr. Sect. B: Struct. Crystallogr. Cryst. Chem.,* 1970, **26(7)**, 1046-1048.

49. R. D. Shannon. *Acta Crystallogr. Sect. A: Cryst.Phys. Diffr. Theor. Gen. Crystallogr.,* 1976, **32(5)**, 751-767.

50. A. K. Singh. *Methods and Applications in Fluorescence,* 2020, **8(4)**, 045008.

51. M. N. Islam, J. Podder and M. L. Ali., *RSC Adv.,* 2021, **11**, 39553-39563

52. L Schimka, R Gaudoin, J Klimeš, M Marsman and G Kresse, *Physical Review B.,* 2013, **87(21)**, 214102.

53. J. P. An, H. Y. Jiang, Y. Tian, H. T. Xue and F. L. Tang, *Physical Chemistry Chemical Physics,* 2019, **21(42)**, 23552-23558.

54. K. Heidrich, W. Schafer, M. Schreiber, J. Söchtig, G. Trendel, J. Treusch, T. Grandke and HJ. Stolz, *Phys. Rev. B,* 1981, **24**, 5642.

55. L. Z. Wang, Y. Q. Zhao, B. Liu, L. J. Wu and M. Q. Cai, *Physical Chemistry Chemical Physics: PCCP,* 2016, **18(32)**, 22188-95.

56. J. Liu, Q. Y. Jiang, S. D. Zhang and H. Zhang, *Physics Letters A,* 2019, **383(34)**, 125990-125990.

57. A. AlQurashi and C.R. Selvakumar, *Superlattices and Microstructures,* 2018, 118308-318.

58. J. Y. Xi , M. Q. Long, L. Tang, D. Wang and Z. G. Shuai, *Nanoscale,* 2012, **4(15)**, 4348-69.

59. Y. Q. Jin, X. D. Wan, M. J. Yao, D. Qiu, D. J. Singh, J. Y. Xi, J. Yang and L. L. Xi, *npj Computational Materials,* 2023, **9(1)**, 190.

60. C. Motta and S. Sanvito, *Journal of Physical Chemistry C,* 2018, **122**, 1361-1366.

61. Y. Kang and S. Han, *Physical Review Applied,* 2018, **10(4)**, 044013.

62. L. K. Ping, M. A. Mohamed, A. K. Mondal, M. F. M. Taib, M. H. Samat, D. D. Berhanuddin, P. S. Menon and R. Bahru, *Micromachines,* 2021, **12(4)**.

63. M. P. Hughes, K. D. Rosenthal, R. R. Dasari, B. R. Luginbuhl, B. Yurash, S. R. Marder and T. Q. Nguyen, *Adv. Funct. Mater,* 2019, **29(29)**, 1901269.

64. X. Liu, B. Xie, C. H. Duan, Z. J. Wang, B. B. Fan, K. Zhang, B. J. Lin, F. J. M. Colberts, W. Ma, R. A. J. Janssen, F. Huang and Y. Cao, *Journal of Materials Chemistry A,* 2018, **6(2)**, 395-403.

65. J. P. An, H. Y. Jiang, Y. Tian, H. T. Xue and F. L. Tang, *Physical Chemistry Chemical Physics*, 2019, **21(42)**, 23552-23558.

66.  Z. Xu, Y. P. Li, C. X. Li and Z. T. Liu, *Journal of Alloys and Compounds,* 2016, **687**, 168-173.

67.  M. Roknuzzaman, J. A. Alarco, H. Wang and K. Ostrikov, *Comput. Mater. Sci.,* 2021, **186**, 110009.

# Data availability statements

The authors confirm that the data supporting the findings of this study are available within the article.

Professor Dr. Yu Qiu

*Key Laboratory of Green Perovskites Application of Fujian Province Universities*
*Fujian Jiangxia University*
*Fuzhou 350108, China*
*Tel: +86-591-23531356, Fax: +86-591-23531375*
*E-mail: yuqiu@fjjxu.edu.cn*